Supporting Information

Photocontrolled Heterojunctions Constructed from Holmium Single Atom Modified $Mg_{1.2}Ti_{1.8}O_5$/g-C_3N_4 with Enhanced Photocatalytic CO_2 Conversion

Jing An, Shuang Ge, Guofeng Wang*, and Honggang Fu*

Table of Contents

Experimental Procedures

Chemicals

All reagents and solvents, including analytical-grade magnesium acetate, tetrabutyl peptide, urea, ethanol, and $Ho(NO_3)_3 \cdot 6H_2O$, were used as received without further purification.

Characterizations

The morphology and size of the samples were analyzed by transmission electron microscope (TEM, JEM-2100, Japan) and scanning electron microscopy (SEM, Hitachi, S-4800). X-ray diffraction (XRD) patterns were recorded on a Bruker D8 Advance diffractometer equipped with Cu Kα radiation (λ = 1.5406 Å, 40 kV, 40 mA).

Atomic force microscopy (AFM) images were performed using an atomic force microscope (SPA-400, Japan). Fourier transforms infrared (FTIR) spectra were measured on a Perkin-Elmer Spectrum One FTIR spectrometer using the KBr particle method. UV-Vis absorption spectra were recorded on a UV spectrophotometer (SHIMADZU UV-2550) in the wavelength range of 200-800 nm. Photoluminescence (PL) spectra were measured using a Hitachi F-4600 fluorescence spectrophotometer equipped with a 150 W Xe lamp. X-ray photoelectron spectroscopy (XPS) analysis was performed on a Thermo Fisher Scientific K-Alphae spectrometer (Waltham, MA, USA) employing a monochromatic Al Kα X-ray source (hν = 1486.8 eV). In situ-XPS analysis was proformed on a ThermoFischer ESCALAB 250Xi spectrometer after exposing the samples to visible or ultraviolet light for 5 hours. High Angle Annular Dark Field Image-Scanning Transmission Electron Microscope (HAADF-STEM) images with atomic resolution were investigated using a JEM-ARM300F transmission electron microscope (TEM) equipped with a probe spherical aberration corrector.

Methods

Section S1. Synthesis of $Mg_{1.2}Ti_{1.8}O_5$ and $Mg_{1.2}Ti_{1.8}O_5:Ho^{3+}$.

A certain amount of $Mg(CH_3COO)_2 \cdot 4H_2O$ was evenly dissolved in 30 ml ethanol solution, and then 950 μl $Ti(OC_4H_9)_4$ was rapid added into the above solution. After continuous stirring for 1 hour, the mixed solution was transferred to a high-pressure reactor, calcined at 180 °C for 24 hours. After cooling to room temperature, the product was washed with ethanol for three times and then dried at 60 °C. The dried powder were ground and placed in a muffle furnace and calcined at 600 °C for 2 hours at a heating rate of 1 °C/min, then naturally cooled to room temperature to obtain the $Mg_{1.2}Ti_{1.8}O_5$ sample. The synthesis process of $Mg_{1.2}Ti_{1.8}O_5:Ho^{3+}$ is similar to that of $Mg_{1.2}Ti_{1.8}O_5$, except that magnesium acetate are replaced by $Ho(NO_3)_3 \cdot 6H_2O$ in the initial reaction stage.

Section S2. Synthesis of ultra-thin g-C_3N_4 and g-$C_3N_4:Ho^{3+}$ nanosheets.

First, 35 g urea was put into a 100 mL covered crucible and heated at 550 ºC in Muffle furnace (at a rate of 0.5 ºC/min) for 3 h. After natural cooling to room temperature, the

obtained light yellow powder was carefully ground evenly. The ground sample was labeled as g-CN. To further obtain ultra-thin g-C_3N_4 nanosheets, 1 g of the synthesized g-CN was placed in an open ceramic vessel and calcined for a second time at 550 ℃ for 2 h. After cooling to room temperature, the powder was ground again and added into three bottles containing 100 mL 2 M HNO_3 solution, refluxed at 120 ºC for 2 hours. The reflux products were naturally cooled to room temperature, washed with deionized water for 5 times to neutral, and finally washed with ethanol for 3 times to obtain ultra-thin g-C_3N_4 nanosheets, labeled as CN. The synthesis process of CN:Ho^{3+} is similar to that of CN, except that $Ho(NO_3)_3 \cdot 6H_2O$ is added into the reaction solution in the initial reaction stage.

Section S3. Synthesis of $Mg_{1.2}Ti_{1.8}O_5$:Ho/g-C_3N_4:Ho. For the chemisorption method, a certain mass of g-C_3N_4:Ho was added into methanol solution, and completely dispersed through ultrasound for 30 min. Then a certain mass of $Mg_{1.2}Ti_{1.8}O_5$:Ho was added to the above solution and continue ultrasound for 30 min. Finally, the product was thoroughly stirred until the solvent completely evaporated. For the in-situ synthesis, the prepared ultra-thin g-C_3N_4:Ho nanosheets was add into the mixed solution of $Ti(OC_4H_9)_4$ and $Mg(CH_3COO)_2 \cdot 4H_2O$, and further stirred for 30 min. The above mixed solution was transferred to a reactor and calcined at 180 ºC for 24 h. After cooling to room temperature, the product was washed with ethanol for three times and then dried at 60 °C. The dried powder were ground and placed in a muffle furnace and calcined at 600 °C for 2 hours at a heating rate of 1 °C/min, then naturally cooled to room temperature to obtain the $Mg_{1.2}Ti_{1.8}O_5$:Ho/g-C_3N_4:Ho. The obtained product is named $Mg_{1.2}Ti_{1.8}O_5$:Ho/g-C_3N_4:Ho-SS. It is noted that the photocatalytic performance of the optimized $Mg_{1.2}Ti_{1.8}O_5$:Ho/g-C_3N_4:Ho-SS sample by the in-situ synthesis was lower than that of $Mg_{1.2}Ti_{1.8}O_5$:Ho/g-C_3N_4:Ho by the chemisorption method, which can be attributed to the destruction of the ultra-thin structure of CN during in situ synthesis.

Section S4. X-ray absorption spectroscopy (XAFS) measurements.

The XAFS study was performed at the BL14B2* of SPring-8 (8 GeV, 100 mA), Japan, in which, the X-ray beam was mono-chromatized with water-cooled Si (111) double-crystal monochromator and focused with two Rh coated focusing mirrors with the beam

size of 2.0 mm in the horizontal direction and 0.5 mm in the vertical direction around sample position, to obtain X-ray adsorption fine structure (XAFS) spectra both in near and extended edge. Ho_2O_3 samples were used as references. For Wavelet Transform analysis, the χ(k) exported from Athena was imported into the Hama Fortran code. The parameters were listed as follow: R range, 1 - 4 Å, k range, 0 - 12.0 $Å^{-1}$; k weight, 2; and Morlet function with κ=15, σ=1 was used as the mother wavelet to provide the overall distribution (Reference 1). Data reduction, data analysis, and EXAFS fitting were performed and analyzed with the Athena and Artemis programs of the Demeter data analysis packages (Reference 2) that utilizes the FEFF6 program (Reference 3) to fit the EXAFS data. The energy calibration of the sample was conducted through standard and Ho_2O_3, which as a reference was simultaneously measured. A linear function was subtracted from the pre-edge region, then the edge jump was normalized using Athena software. The χ(k) data were isolated by subtracting a smooth, third-order polynomial approximating the absorption background of an isolated atom. The *k3*-weighted *χ(k)* data were Fourier transformed after applying a HanFeng window function (Δk = 1.0). For EXAFS modeling, The global amplitude EXAFS (*CN, R,* σ^2 and ΔE_0) were obtained by nonlinear fitting, with least-squares refinement, of the EXAFS equation to the Fourier-transformed data in *R*-space, using Artemis software, EXAFS of the Ho_2O_3 is fitted and the obtained amplitude reduction factor S_0^2 value (0.794) was set in the EXAFS analysis to determine the coordination numbers (*CNs*) in the Ho-O and Ho-N scattering path in sample.

Section S5. Photocatalytic CO_2 reduction measurements.

A certain amount of sample was dispersed into a cylindrical steel reactor with (4 mL) water. The high-purity CO_2 gas enters the reaction device through the water to reach the ambient pressure and further remove the original air and impurities in the reaction device, and achieve the adsorption and desorption balance before irradiation. The samples were continuously irradiated with a light intensity of 455 $mW \cdot cm^{-2}$ using a 300W Xe lamp with a 400 nm cut-off filter for five hours. Quantitative chromatograph (GC2002) was used to analyze and detect the produced gas. In order to ensure the accuracy of the data, all reported photocatalytic reactions have been tested more than

five times. The photocatalytic reaction was carried out for five cycles, and the time of each photocatalytic reaction was 5 hours. For the calculation of the efficiency ratios of samples containing Ho and samples without Ho under different single wavelength light is based on the method reported in the literatures (*ACS Nano,* 2014, *8*, 7229; *JMCA*, 2022, *10*, 5990). First, the calculation of quantum efficiency (QE) for CO and CH_4 generations were calculated using the following equation: QE = (2×CO generation rate + 8×CH_4 generation rate)/(absorption rate of incident photon). And then, the efficiency ratio of g-C_3N_4:Ln^{3+} (Ln = Y, Gd, Eu, Ho) and g-C_3N_4 = (2×CO generation rate + 8×CH_4 generation rate of sample containing Ln)/ (2×CO generation rate + 8×CH_4 generation rate of sample without Ln). Product selectivity of CO = (2×CO generation rate)/(2×CO generation rate + 8×CH_4 generation rate), and product selectivity of CH_4 = (8×CH_4 generation rate)/(2×CO generation rate + 8×CH_4 generation rate).

Section S6. Measurement of photoelectrochemistry.

A CHI 660 electrochemical system (Shanghai Chenhua Instruments, China) was used with a 300 W Xe lamp as the light source, the sample film as the working electrode, saturated Ag/AgCl as the reference electrode, platinum foil as the counter electrode, and 0.5 M Na_2SO_4 aqueous solution for photoelectrochemical measurements. Before testing, the high-purity N_2 was passed through the Na_2SO_4 electrolyte for 30 min. The working electrode was prepared as follows: under vigorous stirring, the prepared photocatalyst (0.1 g) was added to isopropanol (1 mL), and polyethylene glycol (0.05 g) was added for sonication for 10 min. Subsequently, the solution was further vigorously stirred for 30 minutes, to which acetylacetone (0.05 ml) was added, and the resulting solution was maintained under vigorous stirring for one week. 1 cm × 1 cm conductive fluorine-doped tin oxide (FTO)-coated glass was used as the substrate, and the prepared slurry was coated on the substrate by a doctor blade method. The electrodes were dried at room temperature and finally annealed at 150 °C for 2 h in an N_2 atmosphere.

Section S7. Measurement of hydroxyl radicals (•OH).

The coumarin fluorescence probe method analyzed the amount of •OH produced during the photocatalytic reaction. In this system, the photocatalyst (50 mg) was dissolved in

coumarin aqueous solution (0.001 M, 40 mL), mixed well with constant magnetic stirring for 10 min, and irradiated with a 300 W Xe lamp for 1 h. The solution was then centrifuged and the supernatant passed through a filter into a Pyrex glass cell. The resulting solution was analyzed by fluorescence measurement of 7- hydroxycoumarin using a fluorescence spectrophotometer (Perkin-Elmer LS55) at an excitation wavelength of 390 nm.

Section S8. Measurement of transient surface optical voltage (TPV).

The TPV test was carried out by microchip solid-state lasers, instrument type MCA-355-1-30-02-PD. The experimental light source of TPV was laser with wavelength of 355 nm and frequency of 1 KHz. The pulse nanosecond laser was shot into the photomultiplier tube and the sample cell, respectively, with a pulse width of 1.5 ns and an energy of 30 KJ. The laser intensity is adjusted by a gradient circular neutral filter. The photomultiplier tube records the reference signal, and the sample signal is recorded by the digital oscilloscope of the amplifier. The sample pool is made of a material with good shielding against electromagnetic noise. The internal structure of the sample pool from top to bottom is platinum mesh electrode, mica sheet, measured sample, and FTO electrode. The transient photovoltage test (TPV) is also an important means of studying the interfacial charge transfer kinetics of the photocatalyst, and its photovoltage response includes two parts: rise and fall. The increase in photovoltage corresponds to an increase in the concentration of electrons on the conductive substrate of the FTO electrode, and this process is caused by the diffusion of photogenerated electrons to the substrate. While the decrease in photovoltage mainly corresponds to the recombination process of electrons leaving the conductive substrate.

Section S9. Femtosecond transient absorption measurements.

Femtosecond transient absorption (fs-TA) measurements were performed on a Helios (Ultrafast systems) spectrometers using a regeneratively amplified femtosecond Ti:sapphire laser system (Spitfire Pro-F1KXP, Spectra-Physics; frequency, 1 kHz; max pulse energy, ~8 mJ; pulse width, 120 fs) at room temperature. Finally, the data were analyzed through commercial software (Surface Xplorer, Ultrafast Systems).

Section S10. EPR measurement.

The powdered samples were directly put into the quartz sample tube, placed in the resonator of electron spin resonance spectrometer, and tested after a certain time of light reaction.

Section S11. In-situ FTIR analysis

In-situ Fourier Transform Infrared (FTIR) testing was carried out on Germany Brooke INVENIO S (MCT detector) instrument with an Harrick diffuse reflection in-situ chamber. First, 10 mg sample was loaded into the in-situ infrared cell and then CO_2 and H_2O vapor were introduced through the CaF_2 window on the device. Prior to measurement, the catalyst was degassed at 150 °C for 30 min. The first subsequent test is recorded as 0 minutes. The reaction was carried out by turning on the lamp for 1 h after absorbing 1 h of CO_2 in the darkness. During the reaction process, infrared spectra were taken at the 1, 2, 4, 8, 10, 15, 20, 30, 50, and 60 minutes, and carbon dioxide flowed continuously without interruption. Compared with visible light irradiation, the peak intensity of *COOH intermediates produced by the sample under UV irradiation is much higher, indicating a higher catalytic efficiency under UV irradiation, which is consistent with the previous catalytic performance results. In addition, the $*CH_3$ and $*CH_2$ peaks generated under visible light irradiation are slightly stronger than those generated under UV light irradiation, indicating that the product selectivity of CH_4 under visible light irradiation is higher than that under UV light irradiation, which is consistent with the photocatalytic results.

Section S12. Theoretical calculation.

The plane-wave ultrasoft (PWUS) pseudopotential method, as implemented in the Cambridge Sequential Total Energy Package (CASTEP) algorithm, was used to mimic all geometric optimizations, band structure, and the partial density of states (PDOS), work function, and charge density difference. The absorption spectra were obtained in CASTEP using the Perdew-Wang from 1991 (PW91) functional within the generalized gradient approximation (GGA). Furthermore, on-site Coulomb interactions are included for f orbital of Ho (U = 6 eV) using the GGA+U method. The plane-wave expansion's cutoff energy was set to 700 eV. The Brillouin zone integration was

performed with 3 × 4 × 1 k-points for geometry optimization. The criteria for convergence in the total energy, force, and displacement convergence threshold are 1.0×10^{-5} eV/atom, 0.05 eV/Å, and 0.005 Å, respectively. Geometry optimization, electronic structure, and optical property calculations were all performed using spin-polarized magnetic computation. The Gibbs free energy change in photocatalytic CO_2 reduction is defined as $\Delta G = G\text{ (final state)} - G\text{ (initial state)} = E_{reaction} + \Delta E_{zero} - T\Delta S$, where $E_{reaction}$ refers to the reaction energy, E_{zero} is zero vibration energy correction, ΔS represents the differences in entropy, and the reaction temperature is T.

Section S13. The effects of rare earth ions and heterojunctions are different for materials with different compositions and light wavelengths.

(i) For MTO:Ho/1-CN:Ho, the content of MTO:Ho and CN:Ho is the same, with a mass ratio of 50%. However, for MTO:Ho/9-CN:Ho, the content of MTO in the samples is particularly low, only 10%. It is noted that the effect of Ho single atom on the photocatalytic performance of CN under visible light irradiation is much greater than that under UV light irradiation, as shown in Table S2 and Table S6. For MTO:Ho/9-CN:Ho, the CN:Ho content is particularly high, and Ho single atoms have little effect on the photocatalytic performance of CN under UV irradiation, resulting in no significant improvement in the performance of the MTO:Ho/9-CN:Ho. Therefore, this is a normal phenomenon. (ii) For the "Ho single atoms have little effect on the photocatalytic performance of CN under UV irradiation": Ho single atoms are not active sites, and active sites are still mainly distributed on the surface of g-C_3N_4. Therefore, the main role of Ho in catalyst performance includes the generation of more N vacancies by Ho single atoms and the improvement of light utilization efficiency by 4f energy levels. The phenomenon that the effect of Ho on the performance of CN is more significant in the visible light range than in the UV range may be related to the lower transition probability of $^5I_8\rightarrow{}^5G_3(^3H_6)$ and $^5I_8\rightarrow{}^3K_7(^5G_4)$ of Ho^{3+} ions in CN:Ho. The specific reasons for this spectroscopic phenomenon are as follows: According to J-O theory $A_{JJ'} = \frac{64\pi^4 e^2}{3hc^2}\frac{\nu^3}{2J+1}\frac{n(n^2+2)^2}{9}\sum_{\lambda=2,4,6}\Omega_\lambda\langle\Psi' J'\|U^{(\lambda)}\|\Psi J\rangle^2$, the Ω_λ values are related to the local environment around rare earth ions. And thus, the transition probabilities of

$^5I_8 \rightarrow {}^5G_3(^3H_6)$ and $^5I_8 \rightarrow {}^3K_7(^5G_4)$ are related to the local environment around Ho^{3+} ions. Here, due to the relatively weak $^5I_8 \rightarrow {}^5G_3(^3H_6)$ and $^5I_8 \rightarrow {}^3K_7(^5G_4)$ in CN:Ho (Figure S9), Ho cannot effectively improve the UV light utilization of CN, resulting in a less significant performance improvement under UV light irradiation. Therefore, the impact of Ho on CN performance is more significant in the visible range than in the UV. In short, we should acknowledge that the photocatalytic performance of the material still significantly improves after Ho single atom modification. Of course, the extent to which Ho single atoms improve photocatalytic performance depends on many factors such as sample composition and light irradiation wavelength.

Table S1a. The comparison of photocatalytic performance with other reported Ti based catalysts.

Photocatalysts	Reaction solution	Light wavelengths	Production rate (μmol·h^{-1})		References
			CO	CH_4	
Ag/TiO_2	H_2O	λ>400 nm	18.4	46	*Energy Environ. Sci.,* 2024, **17**, 518
Cu/TiO_2	H_2O	PLS-SXE300UV Xe lamp	15.27	0.5	*Angew. Chem. Int. Ed.,* 2022, **61**, e202207600
$CsPbBr_3/Au/TiO_2$	H_2O	Simulate sunlight	17.27	1.22	*J. Am. Chem. Soc.,* 2024, **146**, 3303
$Cs_2AgBiBr_6/Ti_3C_2T_x$	H_2O	λ>400 nm	11.2	1.30	*Appl. Catal. B-Environ.,* 2022, **312**, 121358
TiO_2-$C_3N_4/BiVO_4$	H_2O	λ>420 nm	60	5.18	*Angew. Chem. Int. Ed.,* 2021, **60**, 20906
$SrTiO_3:Er^{3+}/C_3N_4$	MeCN+TEOA	λ>420 nm	23.35	16.90	*J. Mater. Chem. A,* 2021, **9**, 15820
$Mg_{1.2}Ti_{1.8}O_5$:Ho /C_3N_4:Ho	H_2O	λ>420 nm	59.77	9.21	This work
	H_2O	320nm>λ>400nm	100.41	12.60	

Table S1b. The comparison of photocatalytic performance with other RE single atom materials.

Photocatalysts	Reaction solution	Light wavelengths	Production rate (μmol·h^{-1})		References
			CO	CH_4	
Er/C_3N_4	H_2O	λ>420 nm	47.1	2.5	*Angew. Chem. Int. Ed.,* 2020, **59**, 10651
BPEr/SNOEr-10	H_2O	λ>420 nm	19.01	8.89	*Chem. Sci.,* 2024, **15**, 1860
O/La-C_3N_4	Acetonitrile +TEOA+H_2O	Simulate sunlight	92	5.6	*ACS Nano,* 2020, **14**, 15841
$Mg_{1.2}Ti_{1.8}O_5$:Ho /C_3N_4:Ho	H_2O	λ>420 nm	59.77	9.21	This work
	H_2O	320nm>λ>400nm	100.41	12.60	

Table S2. Control experiments to prepare the unexfoliated g-C_3N_4 (g-CN), ultra-thin g-C_3N_4 (CN) nanosheets, Ho single atom anchored ultra-thin g-C_3N_4 (CN:Ho) nanosheets, and their catalytic performance under visible light irradiation.

Samples	Urea	$Ho(NO_3)_3$	Production rate (μmol $h^{-1}g^{-1}$)	
			CO	CH_4
g-CN (unexfoliated)	0.05 mol	0	3.25	2.06
CN (ultrathin)	0.05 mol	0	9.06	3.17
CN:0.1%Ho	0.05 mol	0.05 mmol	21.03	2.55
CN:0.2%Ho	0.05 mol	0.10 mmol	23.75	3.43
CN:0.3%Ho	0.05 mol	0.15 mmol	25.45	3.75
CN:0.4%Ho	0.05 mol	0.20 mmol	22.46	3.45
CN:0.5%Ho	0.05 mol	0.25 mmol	19.21	3.22
CN:0.6%Ho	0.05 mol	0.30 mmol	17.86	3.17
CN:0.7%Ho	0.05 mol	0.35 mmol	16.81	2.77
CN:0.8%Ho	0.05 mol	0.40 mmol	15.47	2.53
CN:0.9%Ho	0.05 mol	0.45 mmol	14.12	2.29
CN:1%Ho	0.05 mol	0.50 mmol	13.08	2.15

Table S3. Control experiments to prepare the $Mg_{1.2}Ti_{1.8}O_5$ and Ho single atom anchored $Mg_{1.2}Ti_{1.8}O_5$, and catalytic performance under ultraviolet light irradiation.

Samples	$Mg(CH_3COO)_2$	$Ti(OC_4H_9)_4$	$Ho(NO_3)_3$	Production rate (μmol $h^{-1}g^{-1}$)	
				CO	CH_4
MTO	0.001250 mol	950 μL	0	48.03	7.25
MTO:0.1%Ho	0.001249 mol	950 μL	0.00125 mmol	50.32	7.56
MTO:0.2%Ho	0.001248 mol	950 μL	0.0025 mmol	52.88	8.29
MTO:0.3%Ho	0.001247 mol	950 μL	0.00375 mmol	60.51	9.98
MTO:0.4%Ho	0.001245 mol	950 μL	0.005 mmol	67.87	11.65
MTO:0.5%Ho	0.001244 mol	950 μL	0.00625 mmol	75.69	13.21
MTO:0.6%Ho	0.001243 mol	950 μL	0.0075 mmol	80.11	15.80
MTO:0.7%Ho	0.001242 mol	950 μL	0.00875 mmol	80.68	15.92
MTO:0.8%Ho	0.001240 mol	950 μL	0.0100 mmol	81.53	15.95
MTO:0.9%Ho	0.001239 mol	950 μL	0.01125 mmol	75.68	17.05
MTO:1%Ho	0.001238 mol	950 μL	0.0125 mmol	70.32	18.03

Table S4. The catalytic performance of different samples under simulated sunlight

irradiation ($320 < \lambda < 780$ nm).

Samples	Production rate (μmol $h^{-1}g^{-1}$)	
	CO	CH_4
CN (ultrathin)	42.62	3.68
CN:0.3%Ho	54.37	4.27
MTO	60.03	8.15
MTO:Ho	91.86	14.35
MTO/9-CN	100.37	8.36
MTO:Ho/9-CN:Ho	141.74	17.07

Table S5. Control experiments to prepare the Ho single atom modified $Mg_{1.2}Ti_{1.8}O_5/C_3N_4$ by the chemisorption method, and catalytic performance under visible light irradiation. Here, the g-C_3N_4 contents in $Mg_{1.2}Ti_{1.8}O_5$/g-C_3N_4 composites are consistent with the initial feeding ratio, which has been proven through elemental analysis.

Samples	MTO:0.8% Ho	CN:0.3% Ho	MTO	CN	MTO:Ho/CN:Ho (or MTO/CN) mass ratios	Production rate (μmol $h^{-1}g^{-1}$)	
						CO	CH_4
MTO:Ho/1-CN:Ho	0.05 g	0.05 g	0	0	1:1	42.9	6.34
MTO:Ho/3-CN:Ho	0.05 g	0.15 g	0	0	1:3	45.38	7.14
MTO:Ho/5-CN:Ho	0.05 g	0.25 g	0	0	1:5	46.87	7.61
MTO:Ho/7-CN:Ho	0.05 g	0.35 g	0	0	1:7	50.53	8.62
MTO:Ho/9-CN:Ho	0.05 g	0.45 g	0	0	1:9	59.77	9.21
MTO:Ho/12-CN:Ho	0.05 g	0.6 g	0	0	1:12	45.51	6.23
MTO/9-CN	0	0	0.05 g	0.45 g	1:9	42.15	4.07

Table S6. Control experiments to prepare the Ho single atom modified CN, MTO, and $Mg_{1.2}Ti_{1.8}O_5/C_3N_4$ synthesized by the chemisorption method, and catalytic performance under ultraviolet light irradiation.

Samples	MTO:0.8 %Ho	CN:0.3%H o	MTO	CN	Production rate (μmol $h^{-1}g^{-1}$)	
					CO	CH_4
g-CN	0	0	0	0.01 g	9.66	2.13
CN	0	0	0	0.01 g	33.97	3.59
CN:0.3%Ho	0	0.01 g	0	0	36.42	2.54

MTO	0	0	0.01 g	0	48.03	7.25
MTO:0.8%Ho	0.01 g	0	0	0	81.53	15.95
5-MTO:Ho/CN:Ho	0.25 g	0.05 g	0	0	75.53	10.64
2-MTO:Ho/CN:Ho	0.1 g	0.05 g	0	0	82.22	11.25
MTO:Ho/1-CN:Ho	0.05 g	0.05 g	0	0	100.41	12.6
MTO:Ho/3-CN:Ho	0.05 g	0.15 g	0	0	49.60	5.22
MTO:Ho/5-CN:Ho	0.05 g	0.25 g	0	0	44.78	4.43
MTO:Ho/7-CN:Ho	0.05 g	0.35 g	0	0	41.60	3.96
MTO:Ho/9-CN:Ho	0.05 g	0.45 g	0	0	35.94	3.25
MTO/1-CN	0	0	0.05 g	0.05 g	50.04	6.42
MTO/9-CN	0	0	0.05 g	0.45 g	32.23	2.52

Table S7. EXAFS fitting parameters at the Ho L_3-edge for various samples.

Samples	Shell	CN^a	R(Å)^b	σ^2(Å^2)^c	ΔE_0(eV)^d	R factor
Ho_2O_3	Ho-O	6*	2.287±0.001	0.0074±0.0013	1.7±0.4	0.0165
	Ho-O	2*	3.194±0.001	0.0048±0.0006	-3.2±0.6	
	Ho-Ho	6*	3.522±0.001			
	Ho-Ho	6*	4.074±0.001	0.0067±0.0011	6.0±1.1	
MTO:Ho/ 9-CN:Ho	Ho-O	8.6±0.6	2.356±0.001	0.0144±0.0011	-2.4±0.1	0.0091
	Ho-N	2.8±0.7	2.445±0.001			

^{a}*CN*, coordination number; ^{b}*R*, the distance to the neighboring atom; $^c\sigma^2$, the Mean Square Relative Displacement (MSRD); $^d\Delta E_0$, inner potential correction; *R* factor indicates the goodness of the fit. $S0^2$ was fixed to 0.795, according to the experimental EXAFS fit of Ho_2O_3 by fixing *CN* as the known crystallographic value. * This value was fixed during EXAFS fitting, based on the known structure of Ho_2O_3. Fitting range: $3.0 \leq k$ (/Å) ≤ 12.0 and $1.1 \leq R$ (Å) ≤ 4.2 (2-Ho); $2.0 \leq k$ (/Å) ≤ 12.0 and $1.0 \leq R$ (Å) ≤ 2.7 (1-Ho). A reasonable range of EXAFS fitting parameters: $0.700 < S_0^2 < 1.000$; $CN > 0$; $\sigma^2 > 0$ Å^2; $|\Delta E_0| < 15$ eV; *R* factor < 0.02.

Table S8. The content ratio of Mg and Ti elements in MTO by ICP testing.

Elements	Mass content	Molar content
Mg	14.620%	0.147%
Ti	44.211%	0.225%

Table S9. The effect of different rare earth ions on the photocatalytic performance of g-C_3N_4 under visible light irradiation. To demonstrate that the effects of different

rare earth ion energy levels on the performance of photocatalysts are different, the most representative elements, including Yttrium (Y), Gadolinium (Gd), Europium (Eu), and Holmium (Ho), were selected as the control group for the experiment for testing. The results indicated that the photocatalytic performance of g-C_3N_4:Eu^{3+} and g-C_3N_4:Ho^{3+} is better than that of g-C_3N_4:Gd^{3+} and g-C_3N_4:Y^{3+}, and g-C_3N_4:Ho^{3+} has the best photocatalytic properties.

Photocatalysts	Main products and rates (μmol g^{-1} h^{-1})		Efficiency ratio of g-C_3N_4:Ln^{3+} (Ln = Y, Gd, Eu, Ho) and g-C_3N_4
	CO	CH_4	
g-C_3N_4	9.06	3.17	1.00
g-C_3N_4:0.3%Y^{3+}	15.05	2.41	1.14
g-C_3N_4:0.3%Gd^{3+}	15.86	2.63	1.21
g-C_3N_4:0.3%Eu^{3+}	18.25	2.54	1.31
g-C_3N_4:0.3%Ho^{3+}	25.45	3.75	1.86

Table S10. The integrated area of the maximum photogenic charge extraction efficiency (corresponding to Figure 4f).

Samples	Max height (absolute value)	Max time (ns*10^5)	Area (absolute value)
CN	1.487	7638	11215
CN:Ho	1.870	2826	13517
MTO	1.262	21540	12572
MTO:Ho	4.097	75858	383078
MTO:Ho/9-CN:Ho	12.745	6054	256685

Table S11. The adsorption energies (E_{adv}), C=O bond lengths, and O=C=O bond angles of CO_2 on the surface of g-C_3N_4 and g-C_3N_4:Ho with different configurations and different adsorption positions. Here, different g-C_3N_4 and g-C_3N_4:Ho configurations correspond to the configurations in Figure S35-S37.

Samples	Site-1	Site-2
g-C_3N_4(I)-CO_2	E_{adv}: -0.07 eV; C=O bond length: 1.178 Å, 1.181 Å; O=C=O bond angle: 178.542 °	E_{adv}: -0.01 eV; C=O bond length: 1.180 Å, 1.180 Å; O=C=O bond angle: 179.119 °

g-C_3N_4(I)-2CO_2	Total E_{adv} for two CO_2 molecules: -0.13 eV; For the CO_2 molecule on the left: C=O bond length: 0.974 Å, 1.181 Å; O=C=O bond angle: 178.824 °	Total E_{adv} for two CO_2 molecules: -0.13 eV; For the CO_2 molecule on the right: C=O bond length: 1.178 Å, 1.181 Å; O=C=O bond angle: 178.796 °
g-C_3N_4:Ho(I)-CO_2	E_{adv}: -0.59 eV; C=O bond length: 1.221 Å, 1.256 Å; O=C=O bond angle: 141.725 °	—
g-C_3N_4(II)-CO_2	E_{adv}: -0.06 eV; C=O bond length: 1.181 Å, 1.179 Å; O=C=O bond angle: 178.923 °	E_{adv}: -0.05 eV; C=O bond length: 1.181 Å, 1.179 Å; O=C=O bond angle: 179.019 °
g-C_3N_4:Ho(II)-CO_2	E_{adv}: -0.08 eV; C=O bond length: 1.180 Å, 1.179 Å; O=C=O bond angle: 178.527 °	—
$Mg_{1.2}Ti_{1.8}O_5$-CO_2	E_{adv}: -0.12 eV; C=O bond length: 1.179 Å, 1.179 Å; O=C=O bond angle: 177.627 °	—
$Mg_{1.2}Ti_{1.8}O_5$:Ho-CO_2	E_{adv}: -0.15 eV; C=O bond length: 1.190 Å, 1.171 Å; O=C=O bond angle: 170.141 °	—

Table S12. Attribution of infrared peaks at different positions.

Positions of infrared peaks	Attribution of infrared peaks	References
3754~3400 cm^{-1}	*H_2O	*Chem. Rev.,* **2019***, 119*, 3962.
2170~2420 cm^{-1}	*CO_2	*Chem. Rev.,* **2019***, 119*, 3962.
1540~1770 cm^{-1}	*COOH	*Chem. Rev.,* **2019***, 119*, 3962.
1026~1079 cm^{-1}	*CHO	*Angew. Chem. Int. Ed.*, **2023**, *62*, e202213124.
1120~1209 cm^{-1}	*CH_3O	*Angew. Chem. Int. Ed.*, **2023**, *62*, e202213124.
1315~1495 cm^{-1}	*CO_3^{2-}	*Chem. Eng. J.*, **2023**, *452*, 139378.
~2074	*CO	*Nat. Catal.*, **2021**, *4*, 719.

2934~2950 cm^{-1}	$*CH_3$	*Adv. Funct. Mater.*, **2024**, *34*, 2308411.
2875~2920 cm^{-1}	$*CH_2$	*Adv. Funct. Mater.*, **2024**, *34*, 2308411.

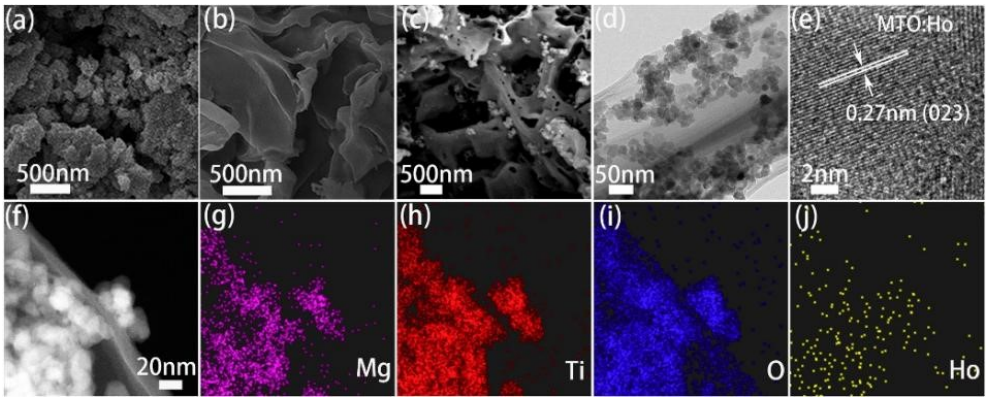

Figure S1. SEM images of (a) MTO, (b) CN, and (c) MTO:Ho/9-CN:Ho. (d-j) TEM, HRTEM, and EDX elemental mappings of MTO:Ho.

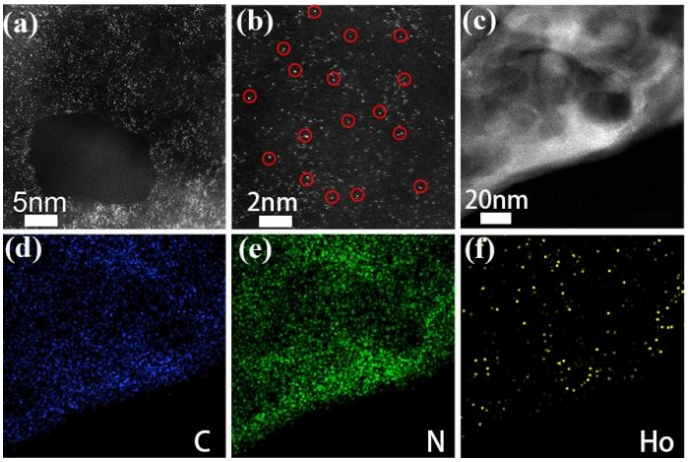

Figure S2. (a,b) AC HAADF-STEM images and (c-f) EDX elemental mappings of CN:Ho.

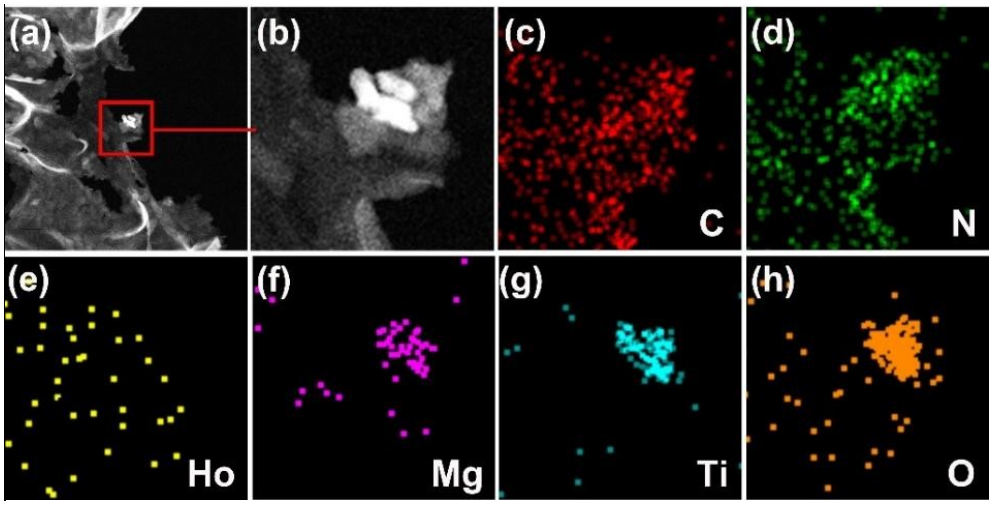

Figure S3. (a) TEM images and (b-h) EDX elemental mappings of MTO:Ho/9-CN:Ho.

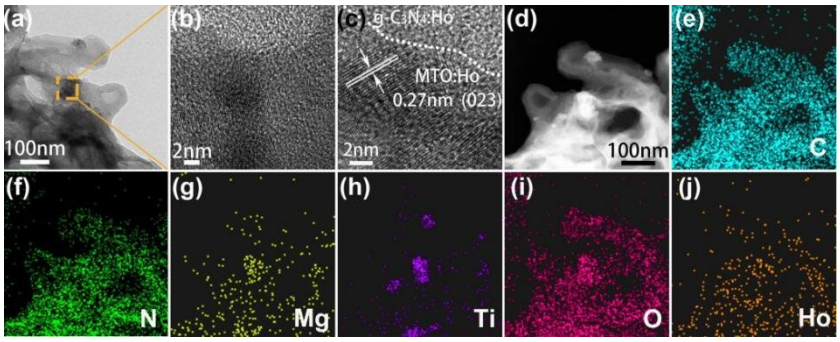

Figure S4. (a-c) TEM and HRTEM images of MTO:Ho/9-g-CN:Ho. (d-j) EDX elemental mappings of MTO:Ho/9-g-CN:Ho. Here, the g-CN:Ho inside MTO:Ho/9-g-CN:Ho was unexfoliated.

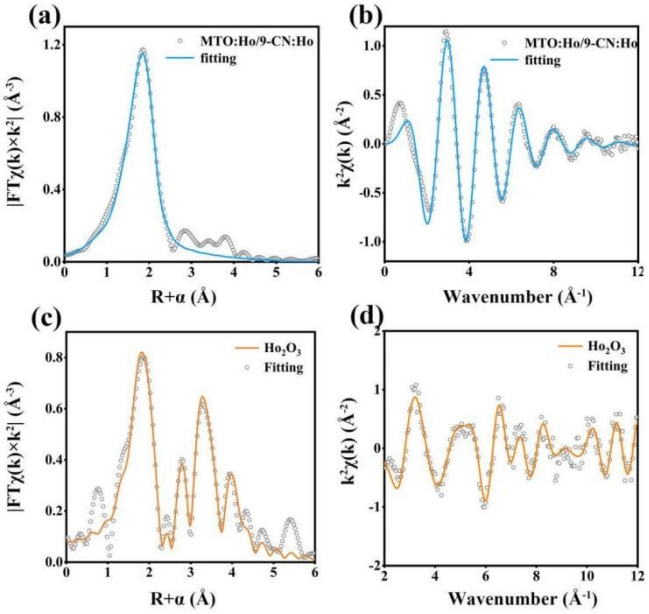

Figure S5. The corresponding EXAFS *R*-space fitting curves and EXAFS k space fitting curves of (a,b) MTO:Ho/9-CN:Ho and (c,d) Ho_2O_3 sample.

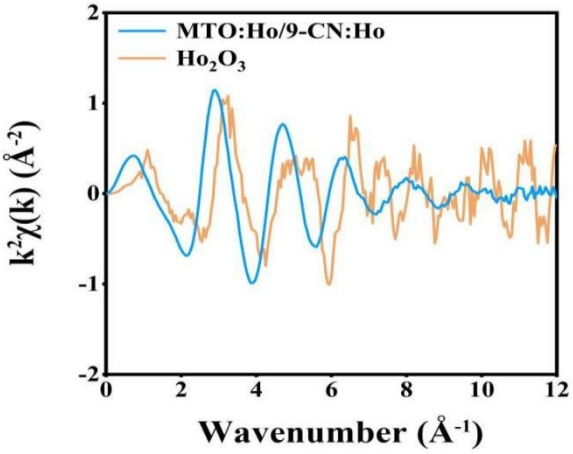

Figure S6. Comparison of the corresponding EXAFS k space fitting curves of MTO:Ho/9-CN:Ho and Ho_2O_3.

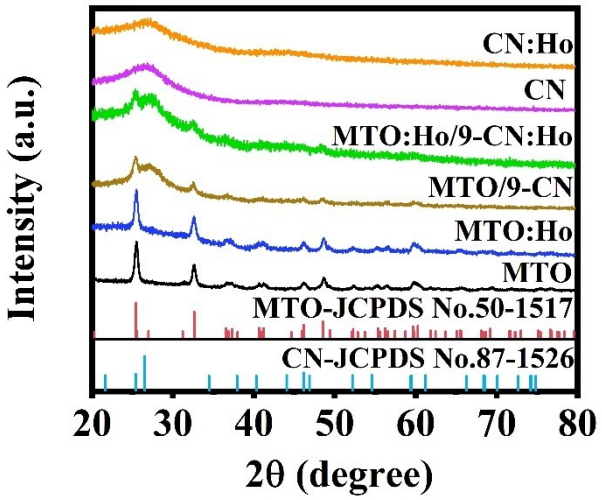

Figure S7. The XRD patterns of different samples.

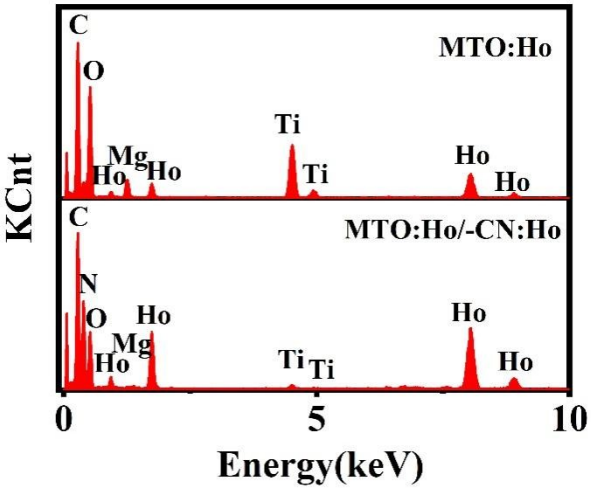

Figure S8. EDS images of MTO:Ho and MTO:Ho/9-CN:Ho.

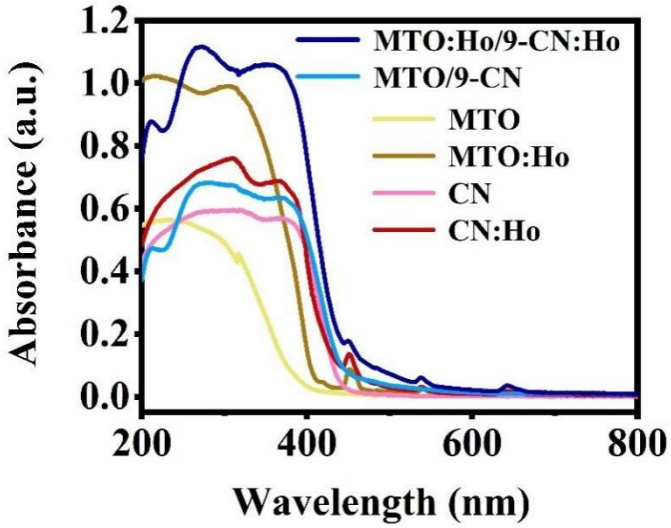

Figure S9. UV-Vis absorption spectra of the different samples.

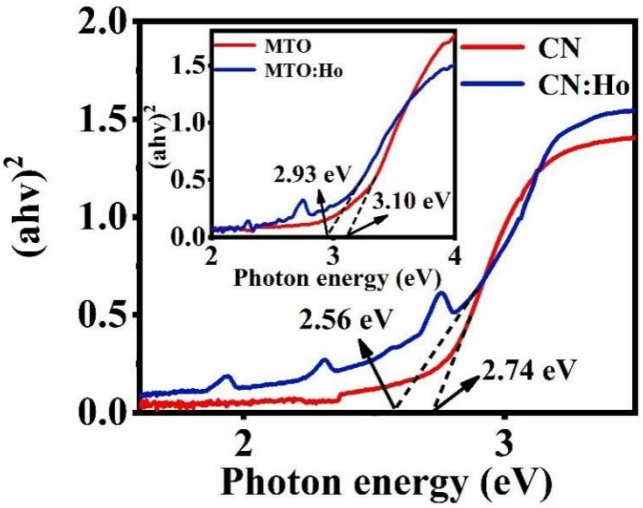

Figure S10. The plots of $(ahv)^2$ versus photon energy.

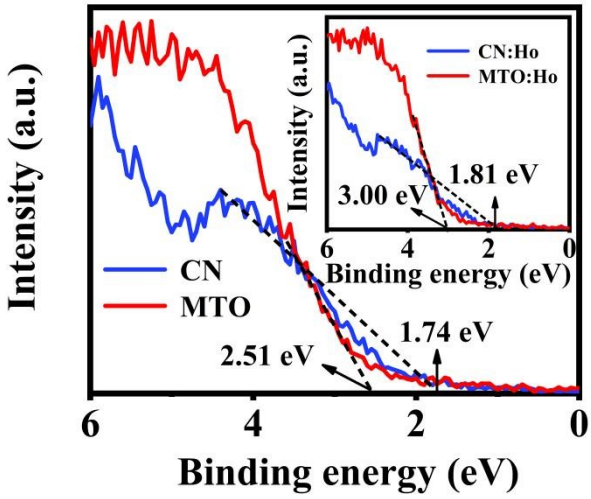

Figure S11. XPS valence band spectra of different samples.

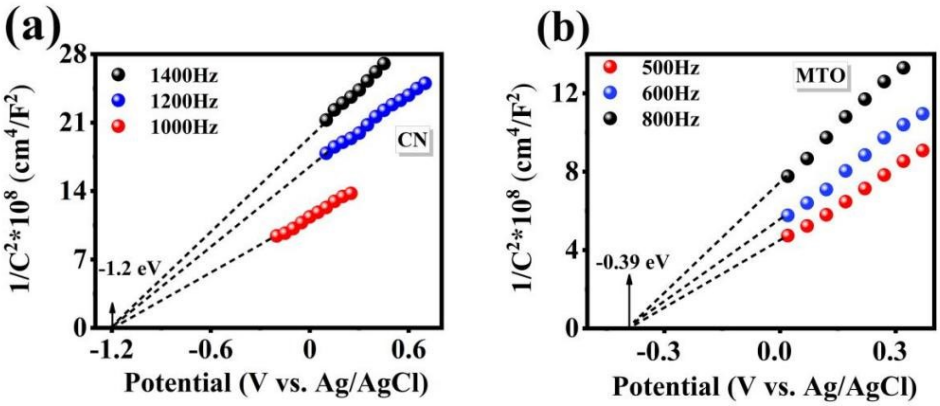

Figure S12. Mott-Schottky plots of (a) CN and (b) MTO.

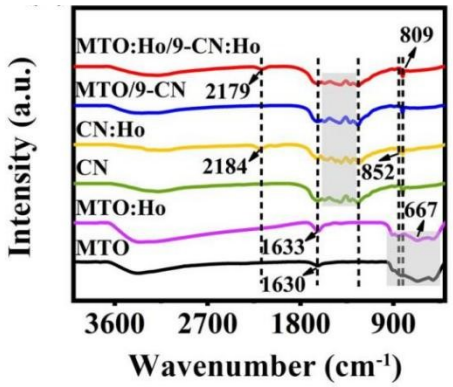

Figure S13. FT-IR spectra of different samples. The peak at ~809 cm^{-1} belongs to the bending vibration of the heptazine heterocyclic ring, and the peak at 1200 cm^{-1}-1650 cm^{-1} belongs to the N-C=N bond and various vibrations of the C-N bond. The new peak at ~2184 cm^{-1} in CN:Ho is related to the telescopic vibration of C≡N. In the spectrum of MTO, the peak at ~500 cm^{-1} belongs to the stretching vibration of Mg-O bond, the peak at 600 cm^{-1}-750 cm^{-1} comes from Ti-O bond, and the peak at 3400 cm^{-1} belongs to the OH vibration of surface water molecules. The characteristic vibration peaks of CN and MTO are observed in the spectra of composite materials.

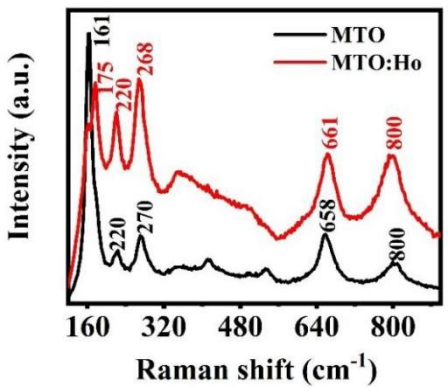

Figure S14. Raman spectra of MTO and MTO:Ho. The peaks at 658 and 800 cm^{-1} are the vibrations of the O atom, and the peaks at 161, 220, and 268 cm^{-1} are attributed to the antisymmetric respiratory vibrations and torsional vibrations of the O octahedron.

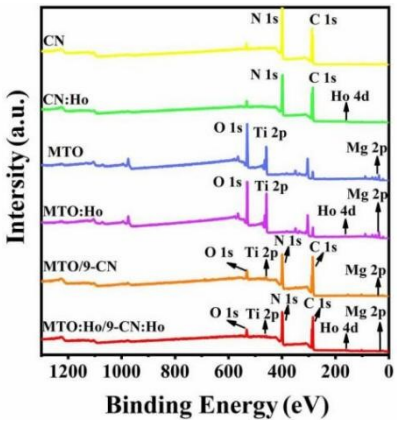

Figure S15. XPS fully scanned spectra of different samples, which can clearly show the elements of each sample, further proving the successful combination of the two materials.

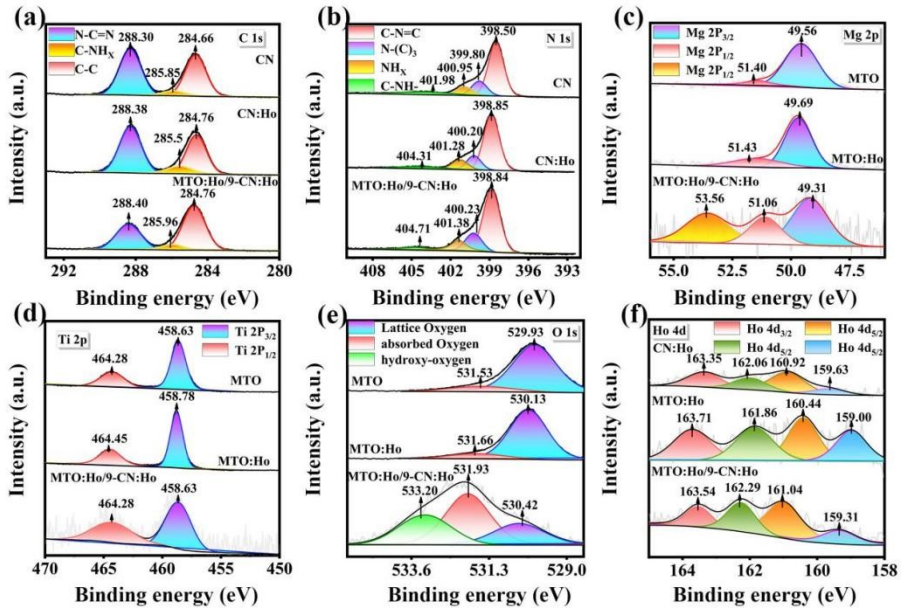

Figure S16. XPS spectra of CN, CN:Ho, MTO, MTO:Ho, and MTO:Ho/9-CN:Ho: (a) C 1s, (b) N 1s, (c) Mg 2p, (d) Ti 2p, (e) O 1s, and (f) Ho 4d.

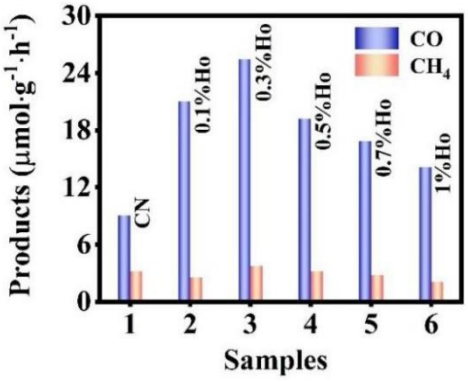

Figure S17. Photocatalytic properties of CN and CN:Ho with different Ho contents under visible light irradiation.

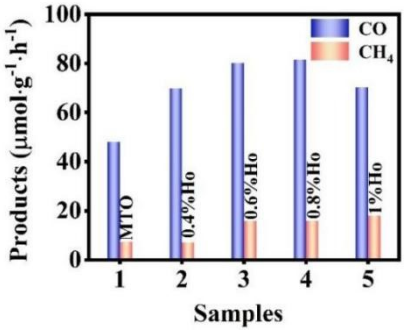

Figure S18. Photocatalytic properties of MTO and MTO:Ho with different Ho contents under ultraviolet light irradiation.

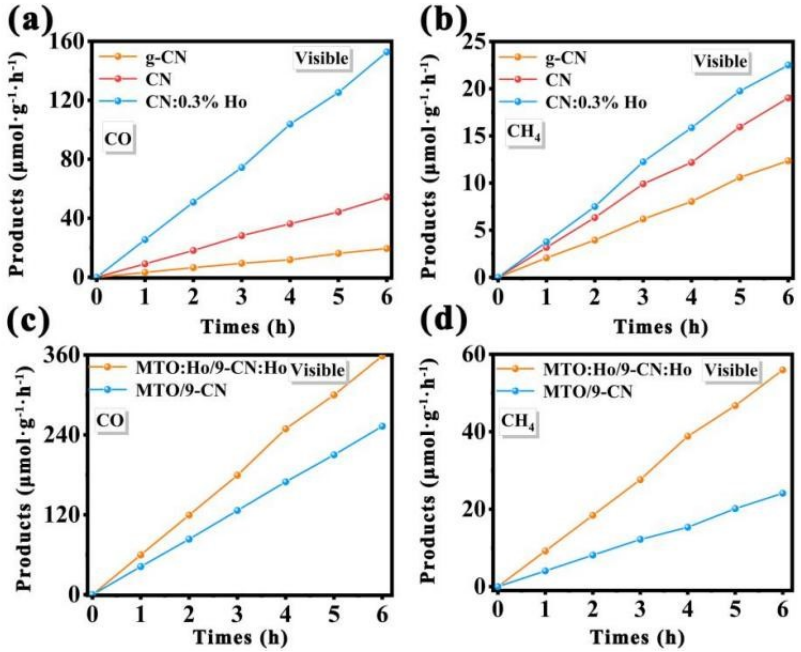

Figure S19. The evolution rates of CO and CH_4 during the photocatalytic CO_2 reduction for the g-C_3N_4, CN, CN:Ho, MTO/9-CN, and MTO:Ho/9-CN:Ho catalysts under visible light irradiation.

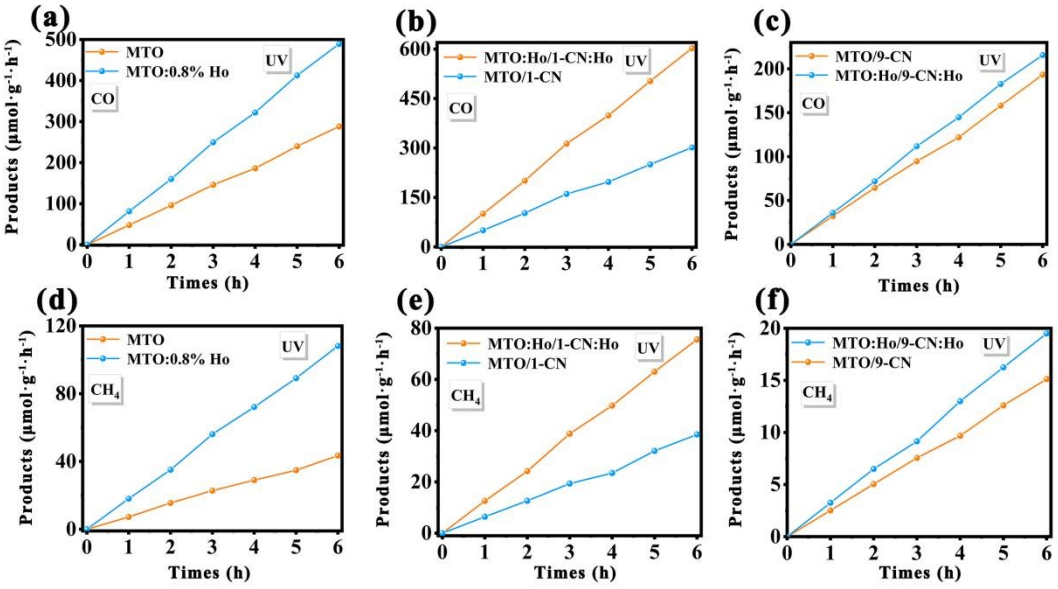

Figure S20. The evolution rates of CO and CH_4 during the photocatalytic CO_2 reduction of the MTO, MTO:Ho, MTO/1-CN, MTO:Ho/1-CN:Ho, MTO/9-CN, and MTO:Ho/9-CN:Ho catalysts under UV light irradiation.

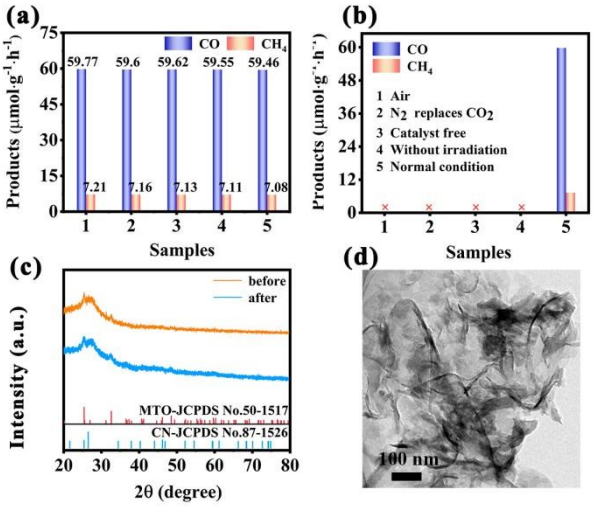

Figure S21. (a) Performance stability of MTO:Ho/9-CN:Ho under visible light irradiation. (b) Performance comparison under different experimental conditions: (1) The content of CO and CH_4 was almost zero when CO_2 was replaced by air for photocatalytic reactions; (2) The yields of CO and CH_4 are zero when CO_2 was replaced by N_2 for photocatalytic reactions; (3) The yields of CO and CH_4 are also zero when there is no catalyst in the catalytic reaction, indicating that the reactor itself cannot decompose CO and CH_4; (4) The yields of CO and CH_4 are zero when there is no light irradiation; (5) For better comparison, the photocatalytic yields of CO and CH_4 for MTO:Ho/9-CN:Ho under normal photocatalytic conditions (corresponding to Figure 2a) are also shown. (c) Comparison of XRD of MTO:Ho/9-CN:Ho before and after photocatalytic reaction. (d) The TEM image of MTO:Ho/9-CN:Ho after photocatalytic reaction, the TEM images of MTO:Ho/9-CN:Ho before photocatalytic reaction are shown in Figure S3.

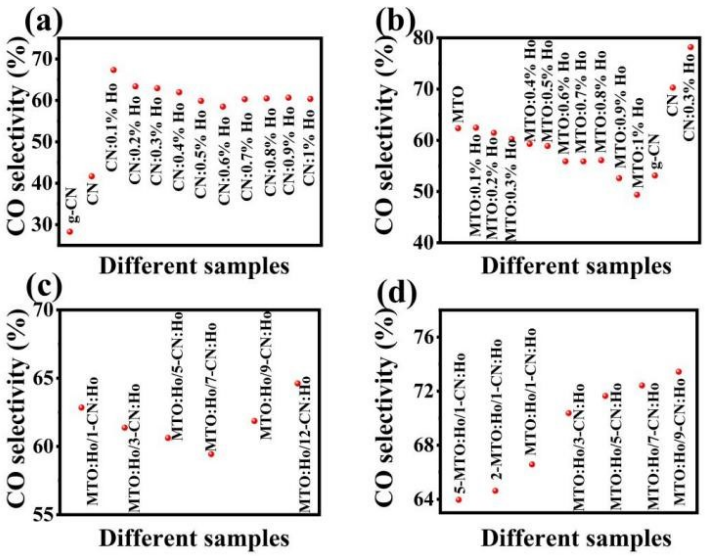

Figure S22. CO product selectivity of different photocatalysts: (a) g-CN, CN, and CN:Ho under visible light irradiation, (b) MTO, MTO:Ho, g-CN, CN, and CN:Ho under UV light irradiation, (c) different composites under visible light irradiation, and (d) UV light irradiation.

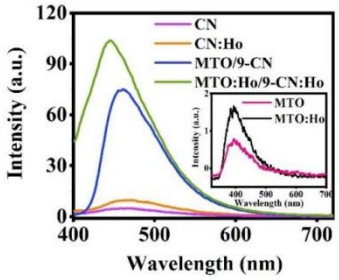

Figure S23. The spectra of hydroxyl radicals under 325 nm light excitation. Here, the hydroxyl radicals of different samples are generated during visible light catalytic processes.

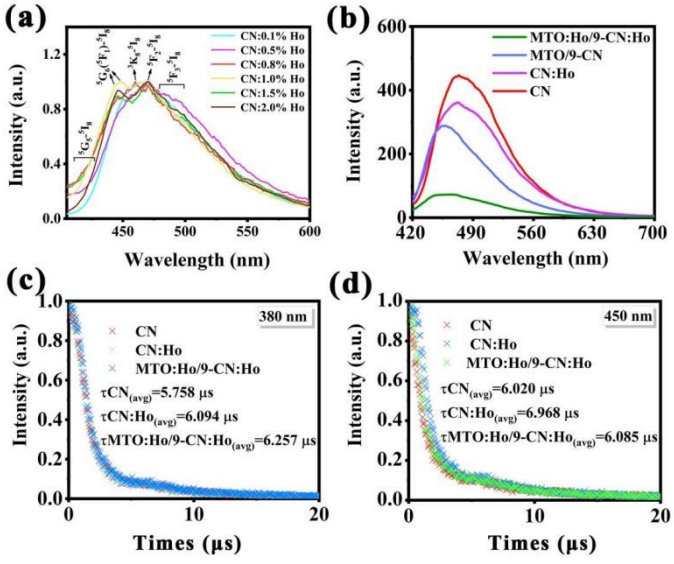

Figure S24. (a) The normalized PL spectra of different samples under 317 nm light excitation (2.5 nm for spectral resolution (FWHM) of the spectrophotometer and 700

V for PMT voltage). (b) PL spectra of different samples under 400 nm light excitation (5 nm for spectral resolution (FWHM) of the spectrophotometer and 400 V for PMT voltage). (c,d) Fluorescence lifetimes (λ_{em} = 480 nm) of different samples excited at 450 nm and 380 nm.

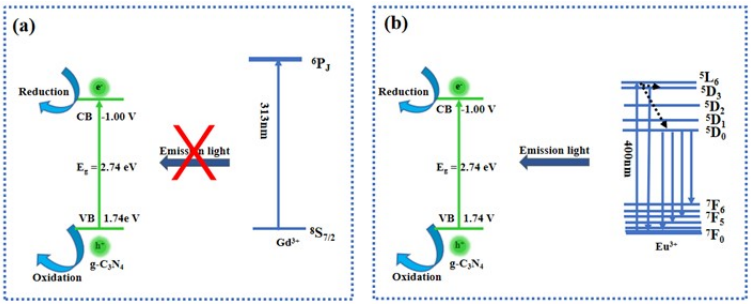

Figure S25. (a) Schematic diagrams of the reason why Gd ions can't help g-C_3N_4:Gd^{3+} absorb visible light. (b) The Schematic diagrams of visible light absorption process of g-C_3N_4:Eu^{3+} assisted by Eu^{3+} ions.

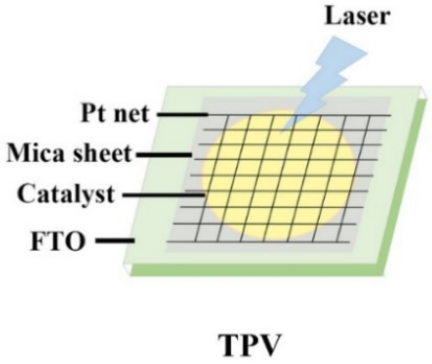

Figure S26. Schematic diagram of TPV test device.

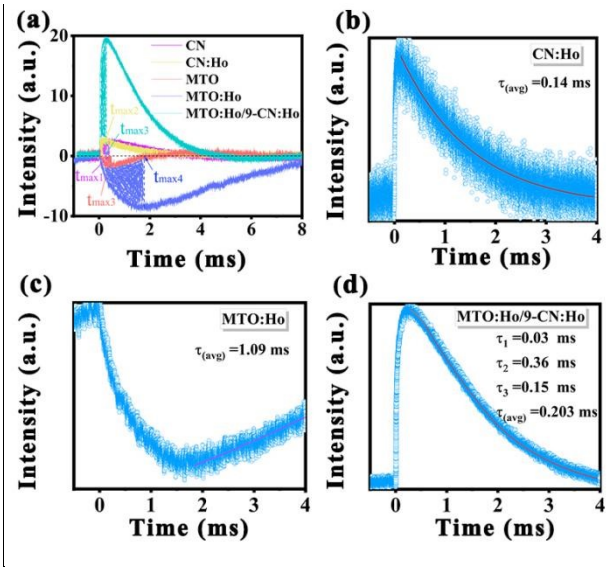

Figure S27. TPV curves of different samples.

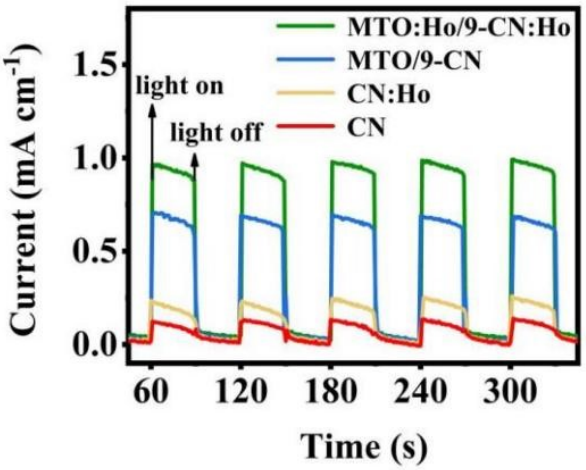

Figure S28. Transient photocurrent curves.

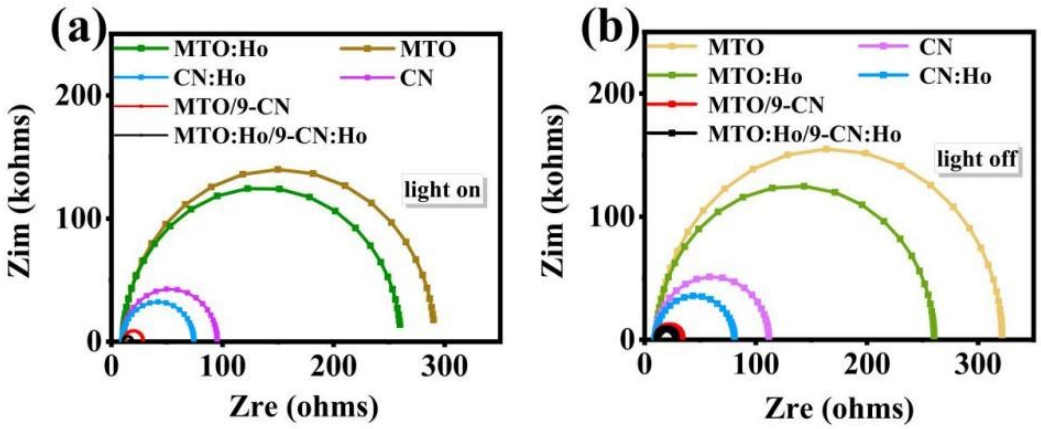

Figure S29. EIS spectra of different samples when light was turned on and turned off.

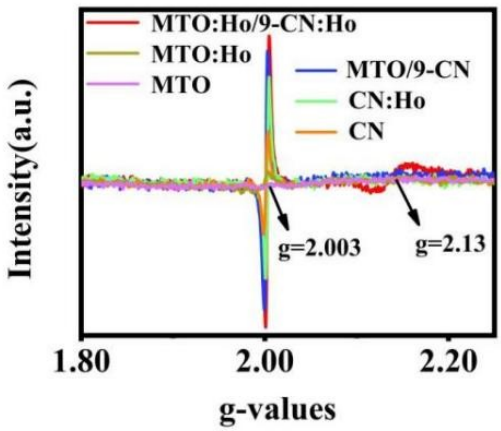

Figure S30. Electron paramagnetic resonance spectra of different samples.

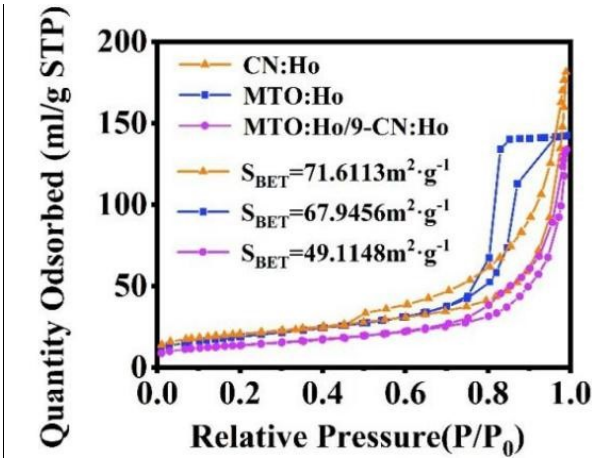

Figure S31. Nitrogen adsorption-desorption isotherms of CN:Ho, MTO:Ho, and MTO:Ho/9-CN:Ho.

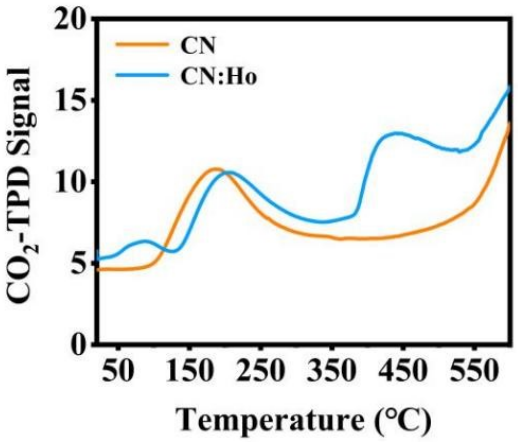

Figure S32. CO_2-TPD profiles of CN and CN:Ho.

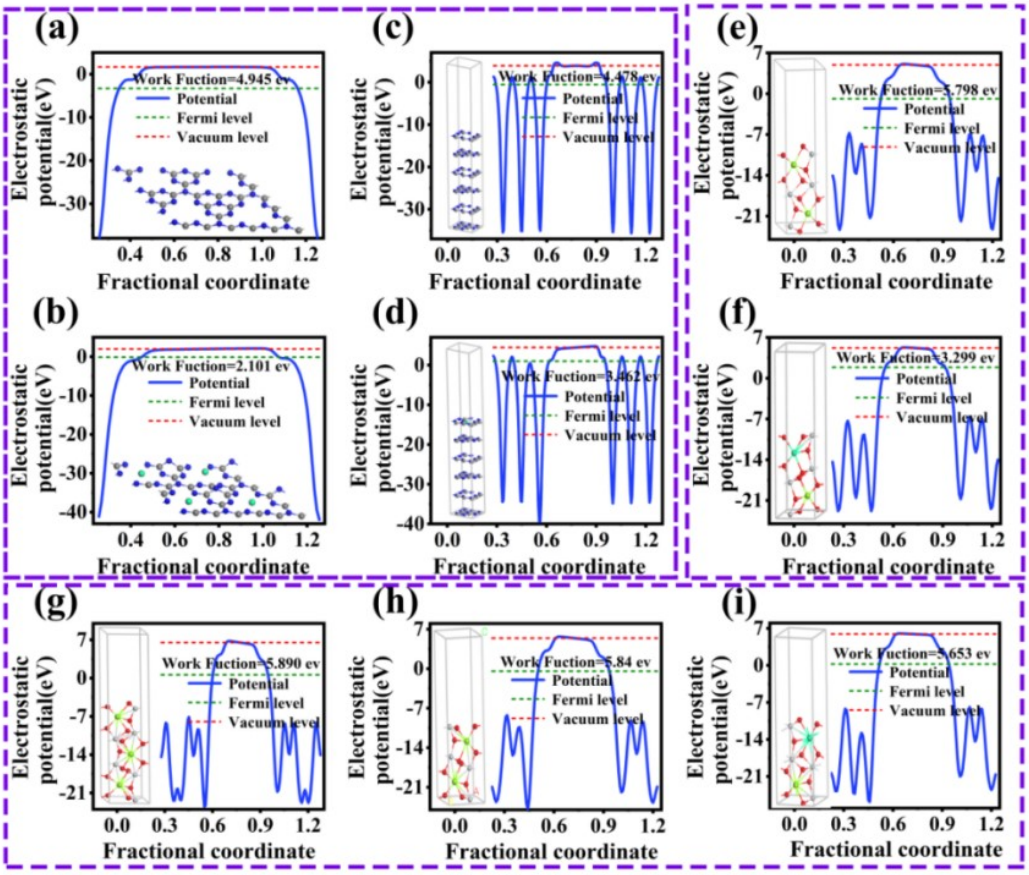

Figure S33. The optimized geometric structures and the calculated work functions of (a,b) single layer CN and CN:Ho, (c,d) multilayer CN and CN:Ho, (e) $MgTi_2O_5$, (f) $MgTi_2O_5$:Ho, (g,h) $Mg_{1.2}Ti_{1.8}O_5$ with different layers, and (i) $Mg_{1.2}Ti_{1.8}O_5$:Ho.

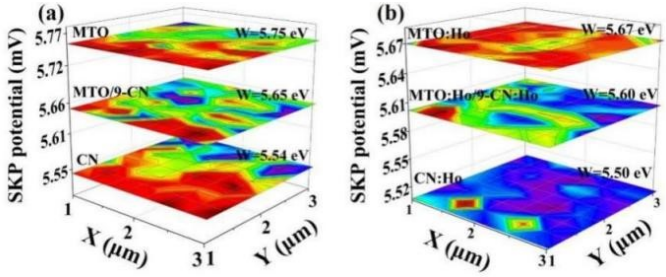

Figure S34. Work function diagrams of different samples.

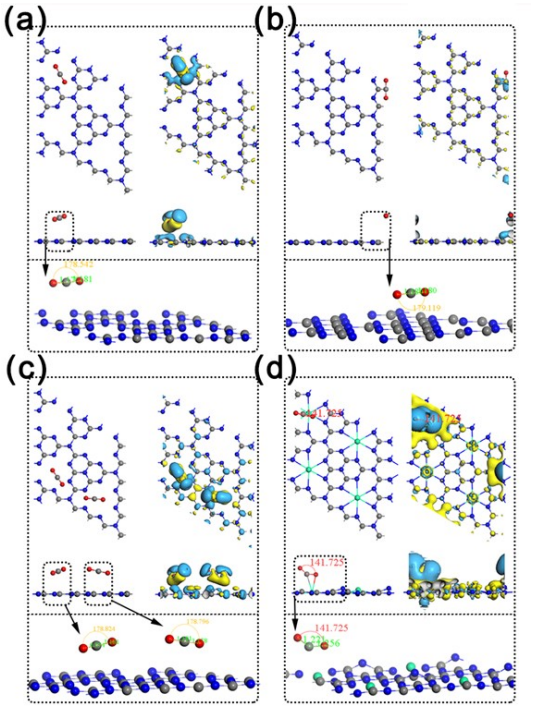

Figure S35. The CO_2 adsorption sites and the charge density difference of the (001) surface of (a-c) g-C_3N_4, and (d) g-C_3N_4:Ho formed by connecting 3-s-triazines as structural units.

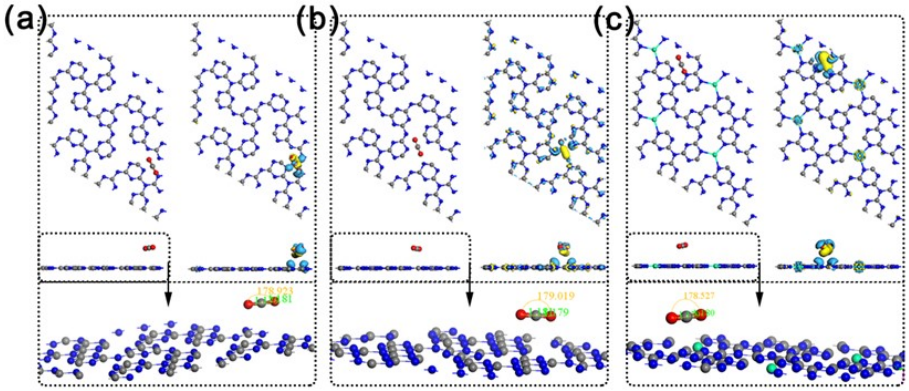

Figure S36. The CO_2 adsorption sites and the charge density difference of the (001) surface of (a,b) g-C_3N_4, and (c) g-C_3N_4:Ho formed by connecting triazine as structural units.

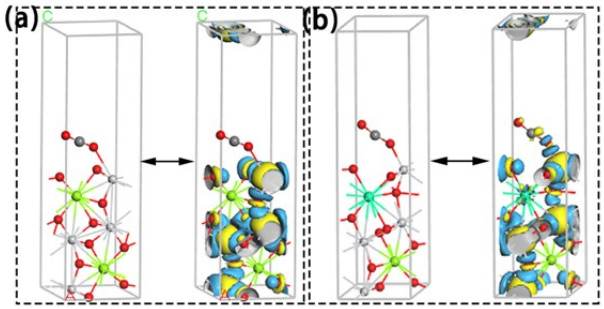

Figure S37. The geometric structures and the charge density difference of CO_2 adsorbed (a) $Mg_{1.2}Ti_{1.8}O_5$ and (b) $Mg_{1.2}Ti_{1.8}O_5$:Ho.

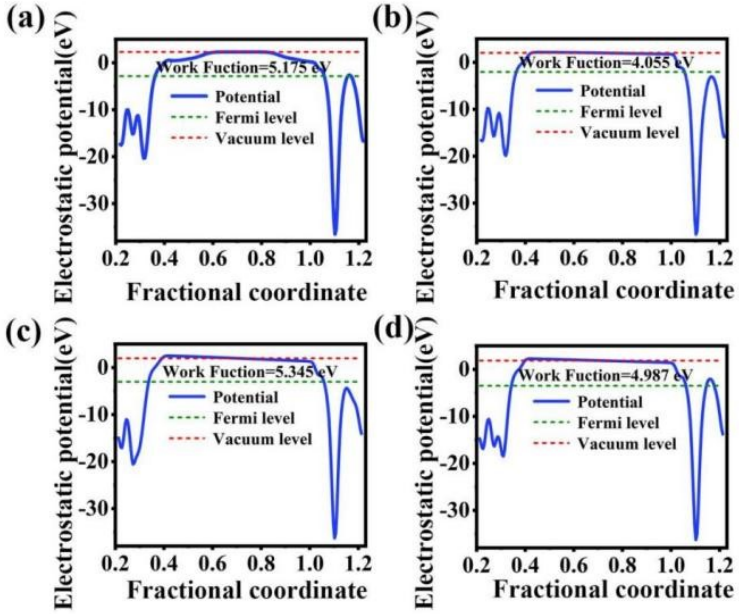

Figure S38. The optimized geometric structures and the calculated work functions of different heterostructures: (a,b) $MgTi_2O_5$/CN and $MgTi_2O_5$:Ho/CN:Ho, (c,d) $Mg_{1.2}Ti_{1.8}O_5$/CN and $Mg_{1.2}Ti_{1.8}O_5$:Ho/CN:Ho.

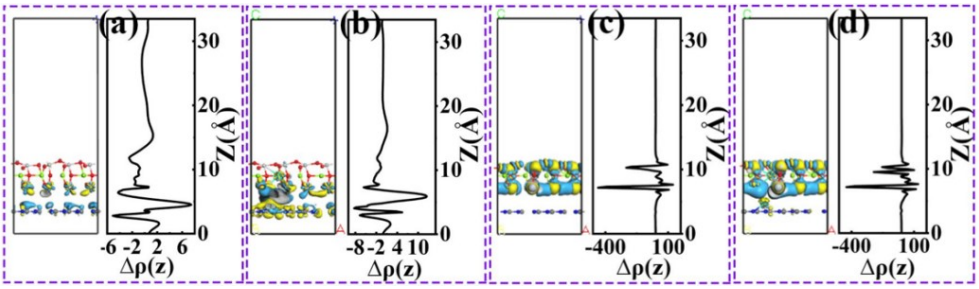

Figure S39. The charge density difference of (e) $MgTi_2O_5$/CN, (f) $Mg_{1.2}Ti_{1.8}O_5$/CN, (g) $MgTi_2O_5$:Ho/CN:Ho, and (h,i) $Mg_{1.2}Ti_{1.8}O_5$:Ho/CN:Ho. The results of the conventional XPS and DFT theoretical calculations indicate that the interface electric field formation at MTO:Ho and CN:Ho interfaces for MTO:Ho/CN:Ho due to the different Fermi levels of MTO:Ho and CN:Ho. Under UV irradiation, the charges are easily transferred from the CB of $Mg_{1.2}Ti_{1.8}O_5$ ($Mg_{1.2}Ti_{1.8}O_5$:Ho) to the VB of CN (CN:Ho) driven by the built-in electric field at the interface.

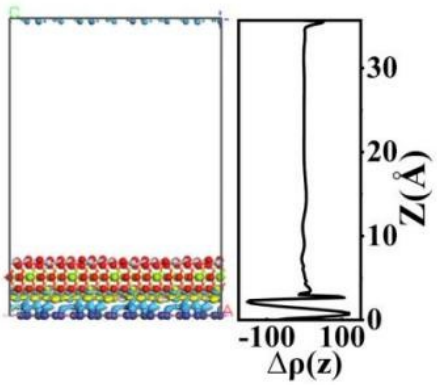

Figure S40. The charge density difference of $Mg_{1.2}Ti_{1.8}O_5$:Ho/CN:Ho.

References：

1. Funke, H.; Scheinost, A. C.; Chukalina, M. Wavelet analysis of extended X-ray absorption fine structure data. Physical Review 2005, B 71, 094110.

2. B. Ravel and M. Newville, ATHENA, ARTEMIS, HEPHAESTUS: data analysis for X-ray absorption spectroscopy using IFEFFIT, Journal of Synchrotron Radiation 12, 537-541 (2005) doi:10.1107/S0909049505012719.

3. Zabinsky, S. I.; Rehr, J. J.; Ankudinov, A.; Albers, R. C.; Eller, M. J. Multiple-Scattering Calculations of X-Ray-Absorption Spectra. Phys. Rev. B 1995, 52 (4), 2995-3009.